Topology Optimization Enables Freeform Matrix Fourier Optics

*Yu-Tzu Liu, Yun-Chien Wu, Chang-Yi Lin, Huan-Teng Su, Yu-Qi Zhou,
and Yao-Wei Huang**

Metasurfaces have revolutionized optics by manipulating light through minute structural modifications, enhancing design flexibility, and reducing conventional optical component size. However, traditional forward design methods often struggle with errors in phase-structure conversion. Inverse design methods, such as topology optimization, directly optimize the structure for desired phase distributions, allowing for almost arbitrary shapes. In this research, a forward design approach is combined with inverse design topology optimization to realize matrix Fourier optics, creating a single-layered metasurface that diffracts incident light of various polarizations to specific positions in the far field, fabricated via atomic layer deposition. It is aimed to optimize diffraction efficiency for each polarization using the adjoint method and gradient descent-based topology optimization, achieving significant improvements in simulations and experiments. The freeform metasurface successfully processed six mixed polarizations, aligning with the matrix Fourier optics concept, demonstrating a polarization contrast of up to 94.4% in numerical and 98.7% in experimental results. Future applications of such polarization-selective gratings can enhance polarization analysis while reducing component size and improving convenience.

1. Introduction

With the discovery of electromagnetic waves, the concept of polarization was introduced into scalar Fourier optics (SFO), aka, diffraction optics.[1] Polarization is widely utilized in nature for tasks such as prey detection, navigation, and communication,[2,3] and it also plays a vital role in scientific fields ranging from astronomy to biomedical diagnostics.[4,5] By incorporating the

Y.-T. Liu, Y.-C. Wu, C.-Y. Lin, H.-T. Su, Y.-Q. Zhou, Y.-W. Huang
Department of Photonics
College of Electrical and Computer Engineering
National Yang Ming Chiao Tung University
Hsinchu 300093, Taiwan
E-mail: ywh@nycu.edu.tw

vectorial nature of light, vector Fourier optics (VFO) extends SFO to describe the electric field as a spatial distribution of Jones vectors, where any arbitrary Jones vector can be expressed as a combination of two orthogonal and mutually independent polarization components.[6] Metasurfaces enable VFO at a subwavelength scale.[7–9] By leveraging both propagation and geometric phases, two distinct phase distributions can be encoded for two arbitrary orthogonal polarization states.[10] However, this approach only enables two functionalities simultaneously and is limited to two orthogonal polarizations. To overcome this limitation, alternative strategies such as vertical stacking[11–14] or spatial multiplexing[15–18] have been proposed to control more than two polarization states. As illustrated in **Figure 1a**, metasurfaces can thus achieve spatially varying polarization responses, yet each meta-atom that supports more than two polarization-encoded functionalities remains constrained.

To enable more generalized spatial control of polarization, Rubin et al.,[19,20] proposed matrix Fourier optics (MFO), which directly applies the Fourier transform to the Jones matrix of a metasurface, thereby enabling multiple polarization states at different diffraction orders (Figure 1b). This advancement allows for full-Stokes polarization imaging with independent control over multiple polarizations,[19] computer-generated Jones matrix holography,[21] and Mueller Matrix imaging.[22] Additionally, the off-diagonal terms of the Jones matrix provide extra functionality through polarization conversion. Up to 11-channel polarization multiplexing has been achieved via optimization,[23] but eliminating holographic image cross-talk still relies on vertical stacking of metasurfaces.[24] Moreover, current MFO implementations primarily rely on forward design, wherein each meta-atom is modeled by a unitary matrix, often overlooking amplitude modulation control. This omission hinders truly independent modulation of amplitude and phase across multiple polarizations.

In this work, we present a topology-optimized freeform metasurface, designed via inverse methods, to realize the MFO concept. As shown in Figure 1c, our metasurface diffracts specific incident-polarized light into six discrete orders, each corresponding to a desired polarization state in the far field. Inverse design uses optimization algorithms to iteratively refine structural

**ADVANCED
SCIENCE NEWS**

www.advancedsciencenews.com

**ADVANCED
OPTICAL
MATERIALS**
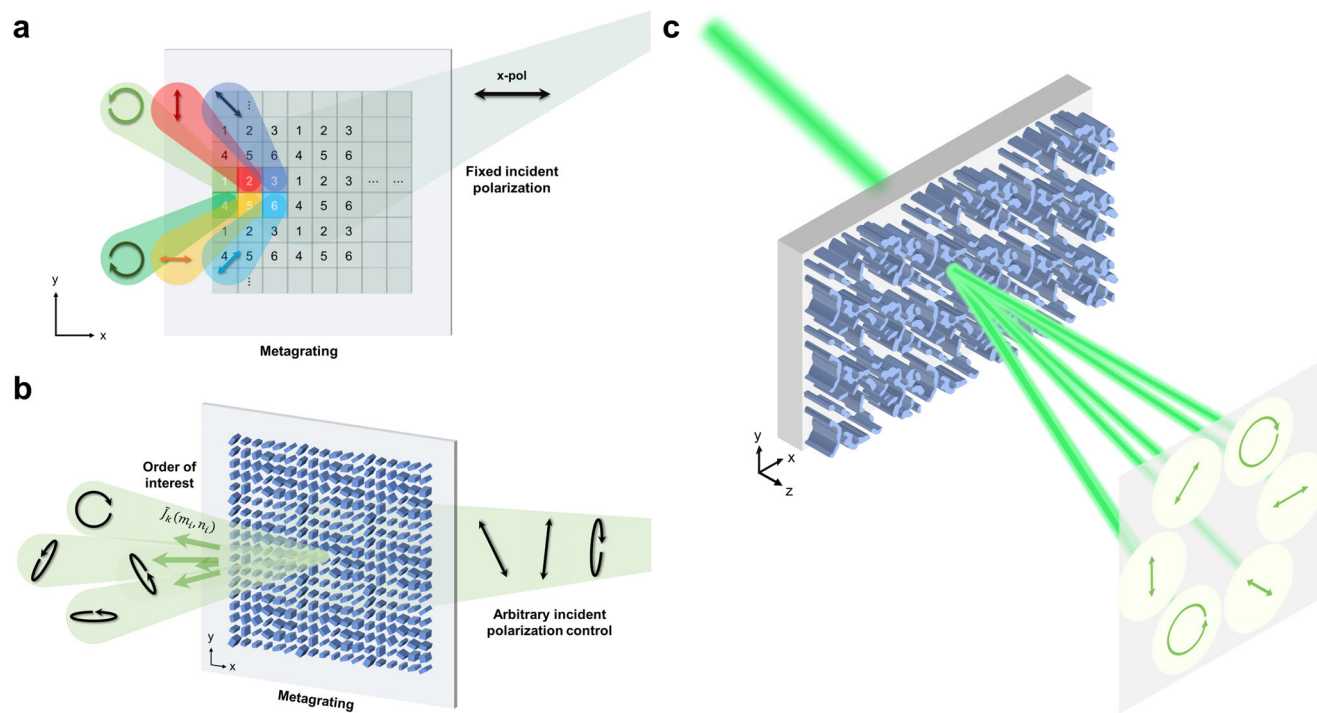
www.advopticalmat.de

Figure 1. Schematic of the Fourier optics in vector and matrix regimes. a) Multiple polarization generation using metasurface with vector Fourier optics. b) Matrix Fourier optics enabled an arbitrary polarization-tunable metasurface. c) Freeform metasurface with matrix Fourier optics that diffracts six polarizations to different diffraction orders.

geometries based on figures of merit (FoM), thereby minimizing design errors and enhancing precision.[25] While machine learning methods excel at complex, non-linear problems, they often require extensive datasets and computationally intensive pre-training.[26,27] Evolutionary algorithms and genetic-type tree optimization enable global optimization but suffer from slow convergence without gradient-based updates.[28–30] In contrast, topology optimization, which relies on gradient descent to refine a refractive index distribution, permits freeform structural configurations with high design flexibility.[31–35] By using the adjoint method[31,36] for efficient gradient calculation, topology optimization becomes particularly well-suited for large-scale metasurface designs. Although topology optimization is prone to local maxima or minima, especially as more functionalities are considered in the FoM, we circumvent this challenge by initializing our inverse design with forward-designed VFO metasurfaces that already satisfy partial requirements for circular and linear polarization (CP and LP) diffraction. This approach ensures a more efficient search for the global optimum and paves the way for high-performance, multi-polarization metasurface designs.

2. Forward Design with Vector Fourier Optics

In the design process, we first modeled rectangular TiO$_2$ nanopillars as meta-atoms, operating at a wavelength of 532 nm. These were arranged in a hexagonal lattice with a 400 nm period and a fixed height (h) of 600 nm, as depicted in **Figure 2a**. The hexagonal configuration reduces aliasing phenomena at high numerical aperture or short wavelengths, suppressing un-

intended diffractions and facilitating efficient control of optical wavefronts.[37] The pillar widths (W_x, W_y) ranged from 100 to 335 nm, providing a practical balance between fabrication feasibility and phase retardation coverage. We then assembled 6 such meta-atoms into a supercell to form a metagrating. The metasurface is optimized to detect 6 key polarization states for full Stock analysis: 4 LPs (horizontal $|H\rangle$, vertical $|V\rangle$, 45° diagonal $|D\rangle$, and 135° anti-diagonal $|A\rangle$) and 2 CPs (left-handed $|L\rangle$ and right-handed $|R\rangle$). The metagrating periodicity was set to 1.2 µm, thereby creating a primary diffraction angle of ≈26.3°.

To construct this metasurface, we defined a rectangular unit cell measuring 2.4 µm ×1.387 µm, effectively doubling the original periodicity to increase the design freedom. Each pair of orthogonal polarization states shares one metasurface design, oriented at azimuthal angles of 0°, 60°, or 120°. For clarity, we describe diffraction orders using Cartesian indices—for instance, (1,0) indicates the 1st order in the x-direction and 0th order in the y-direction. Utilizing the meta-atoms' propagation phase, the output states $|H\rangle$, $|V\rangle$, $|D\rangle$ and $|A\rangle$ were designed to diffract into the (2, 0), (-2, 0), (-1, 1), and (1, -1) orders, respectively. Meanwhile, by leveraging the meta-atoms' geometric phase, $|L\rangle$ and $|R\rangle$ are converted to $|R\rangle$ and $|L\rangle$ and diffracted to the (1, 1) and (-1, -1) orders respectively. Figure 2a illustrates these diffraction orders, their directions, and the corresponding polarization states. And Figure 2b–d shows top-view layouts of the forward-designed nanostructures for the respective cases. Finally, to implement matrix Fourier optics via topology optimization, we overlaid the three forward-designed gratings as our initial configuration, as depicted in Figure 2e.
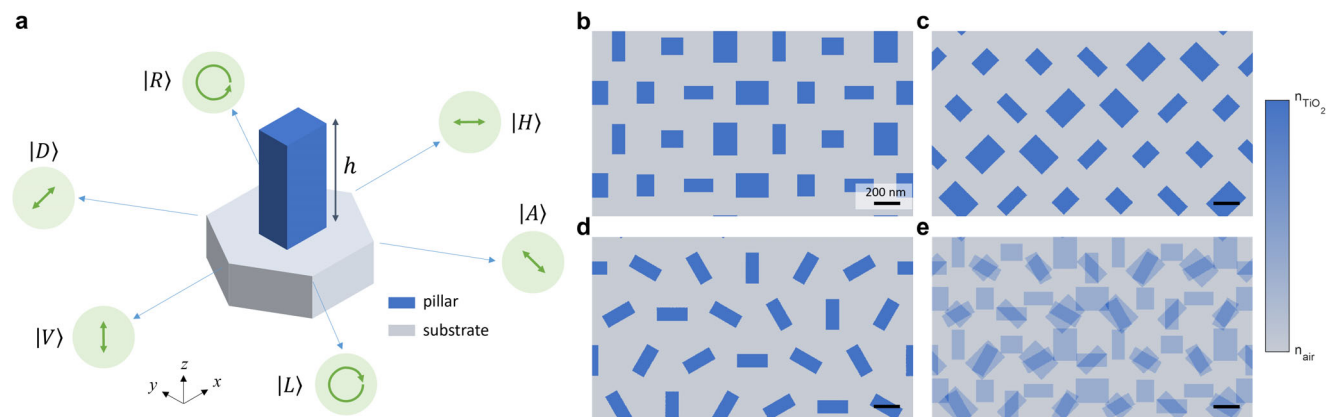
**ADVANCED
SCIENCE NEWS**

www.advancedsciencenews.com

**ADVANCED
OPTICAL
MATERIALS**

www.advopticalmat.de

Figure 2. Schematic of the forward-designed metasurface. a) Meta-atom in a hexagonal lattice and the pre-designed incident polarizations (arrows in the green circle) with their output polarization (expressed in the ket notation) at corresponding diffraction directions. b) Metasurface designed for $|H\rangle$, and $|V\rangle$ using the propagation phase modulation. c) Metasurface designed for $|D\rangle$ and $|A\rangle$ using propagation phase modulation. d) Metasurface designed for $|L\rangle$ and $|R\rangle$ using the geometric phase modulation. e) The initial pattern of the overlapped three forward-designed metagratings.

3. Inverse Design of Matrix Fourier Optics

Our method for designing a freeform metagrating for matrix Fourier optics can be summarized as follows. We employed the topology optimization approach for the inverse design, with the pattern distribution (ρ_0, ranging from 0 to 1) from the forward design as the initial condition, representing the refractive index between air and TiO$_2$. Upon configuring the optimization parameters, the procedure initiates in accordance with the delineations presented in **Figure 3a**. Following each iteration, ρ_0^q, where q indicates the qth iteration, undergoes two rounds of blur and contrast functions, yielding a distribution ρ_4^q (see Section S1 for detailed pattern process, Supporting Information). The process is to ensure fabrication feasibility and drive the material

pattern toward either air or TiO$_2$. Subsequently, we employ rigorous coupled-wave analysis (RCWA)[38] to conduct electromagnetic simulations on the grating, facilitating the derivation of the near-field Jones matrix $J(x, y)$ along with the far-field Jones matrix $\tilde{J}_k(m_i, n_i)$ for specified diffraction orders (m_i, n_i), given by

$$\tilde{J}_k\left(m_i, n_i\right) = \mathcal{F}\left\{J\left(x, y\right)\right\} \tag{1}$$

And we assess the desired diffraction efficiency ($T_{\lambda_i^* \lambda i}$), which is defined as the desired incident polarization state (λ_i) converted to its conjugate (λ_i^*), given by for each incident polarization

$$T_{\lambda_i^* \lambda i} = \left|\left\langle \lambda_i^* \right| \tilde{J}_k\left(m_i, n_i\right) \left| \lambda_i \right\rangle\right|^2 \tag{2}$$
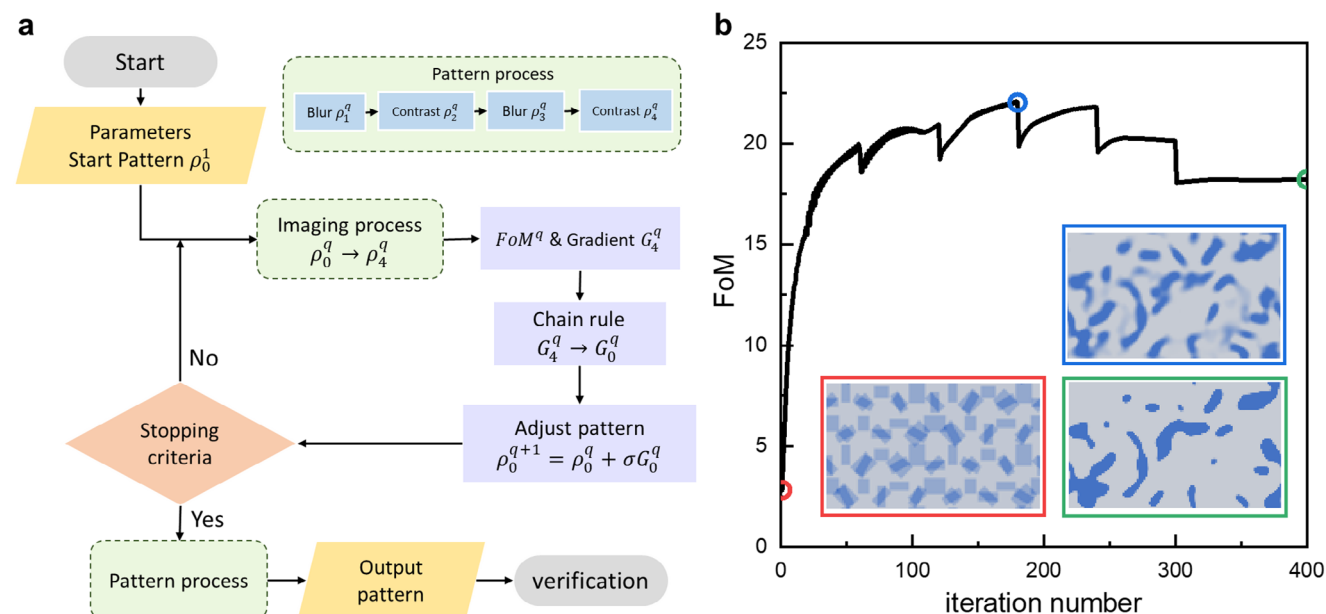

Figure 3. Topology optimization workflow and actual optimization trend. a) Schematic of the optimization flowchart. b) Trend of the FoM with iteration steps and corresponding structure evolution during optimization.

**ADVANCED
SCIENCE NEWS**

www.advancedsciencenews.com

**ADVANCED
OPTICAL
MATERIALS**

www.advopticalmat.de

where (m_i, n_i) indicates the ith order corresponding to its desired input polarization state λ_i, e.g., (2, 0) for T_{HH}, (-2, 0) for T_{VV}, (1, 1) for T_{RL}, (-1, -1) for T_{LR}, (-1, 1) for T_{DD}, and (1, -1) for T_{AA}. The figure of merit of the qth iteration (FoM^q) reflects the average of the 6 desired diffraction efficiency ($N = 6$) during the optimization process, given by

$$FoM^q = \frac{1}{N} \sum_{i=1}^{N} T_{\lambda_i^* \lambda i} \tag{3}$$

We use an adjoint-based topology optimization for gradient calculation.[31,39] The forward simulation provides the near-field electric field and complex amplitudes for the designated diffraction orders. We then executed a backward simulation to reverse compute the adjoint electric field, using the adjoint incident phase determined by those diffractive complex amplitudes from the forward simulation, one forward and one adjoint simulation yields the gradient (G_4^q) for the FoM, which corresponds to the processed pattern (ρ_4^q) and requires adjustment using the chain rule to acquire the gradient (G_0^q) for the original input pattern. Finally, the original input pattern is updated (ρ_0^{q+1}), completing one iteration.

Figure 3b illustrates the variations in the FoM and the pattern distribution within a single unit cell of the grating throughout the 400-iteration optimization process. Key iterations, e.g., the 1st, 180th, and 400th, highlight the design's evolution, and their pattern are shown in the inset of Figure 3b, respectively. By the 180th iteration, the FoM has nearly reached its optimal value but may still be trapped at a local maximum. To provide the optimization process with an opportunity to escape the local maximum, we implemented a deliberate blur every 60 iterations (See Section S2, Supporting Information for a detailed intentional blur introduction). The FoM plateaus after the 180th iteration, showing no significant improvement, indicating that the optimization is either stuck in a local maximum or has already reached the global maximum. We note that the pattern distribution does not exhibit sufficient contrast, making it impossible to realize a gradient refractive index in the experimental pattern. Furthermore, more pairs of blur and contrast functions continue refining the structure until the 400th iteration, ultimately converges to a binary design with only two refractive indices of n_{air} and n_{TiO2}. Occasional sharp dips in efficiency correspond to the intentional blurs aimed at enhancing optimization by evading local maximum. See Section S2 (Supporting Information) for detailed pattern and gradient distribution during the optimization.

Figure 3b illustrates one possible optimization process, but it is by no means the only one. Specifically, it begins with the initial pattern shown in Figure 2e, which is generated by superimposing three gratings. Because there is freedom in how the 3 grating patterns can be overlapped, we fixed the pattern from Figure 2b, shifted the one from Figure 2c by $(\Delta x_1, \Delta y_1)$, and shifted the one from Figure 2d by $(\Delta x_2, \Delta y_2)$ before overlaying them. The parameters $(\Delta x_1, \Delta y_1, \Delta x_2, \Delta y_2)$ thus introduce additional design flexibility. Section S3 (Supporting Information) details the resulting optimization processes, in which we compare efficiencies and polarization contrasts. Based on these evaluations, we selected the pattern in Figure 2e for experimental verification.

4. Experimental Results

We fabricated our freeform metasurface sample using electron-beam lithography, atomic layer deposition (ALD),[40,41] and high-density plasma reactive ion etching (HDP-RIE), as detailed in Section S4 (Supporting Information). **Figure 4a** shows a scanning electron microscope (SEM) image of the fabricated sample, which contains ≈4 unit cells with a structure consistent with the designed freeform metasurface. Figure 4b presents a tilted SEM view revealing a grating height of ≈600 nm. To evaluate the fabricated sample, we made slight modifications to the original design (based on the SEM image) and imported both the original and modified layouts into the finite-difference time-domain (FDTD, Lumerical) solver. Unlike the RCWA method, FDTD can directly accept structural layouts, enabling accurate replication of the patterned geometry as produced in lithography, and thereby allowing more precise analysis of the fabricated freeform structure. Simulations indicate that these minor alterations have a certain impact on diffraction efficiency and polarization contrast, as deliberated in Section S5 (Supporting Information).

Figure 4c displays the diffraction patterns under different incident polarizations (expressed in ket notation), captured using a camera. The red-circled spots correspond to the designed diffraction orders for each incident polarization. However, weaker unintended spots appear at the (±1, 0) and (0, ±1) orders, likely due to the lack of symmetrical constraints (i.e., simulating a hexagonal unit cell with a rectangular unit cell) during optimization. As a result, these additional diffraction orders produce a rectangular lattice in place of the intended hexagonal one. To address this issue, future designs could incorporate hexagonal lattice symmetrical constraints to suppress undesired diffraction orders; however, these constraints might reduce diffraction efficiency or polarization contrast, as discussed in Section S6 (Supporting Information). A detailed analysis of the crosstalk between unintended and target diffraction orders is also provided in Section S7 (Supporting Information).

In the experiment, a power meter was placed at each order corresponding to its target output polarizations, enabling measurement of the sample's desired diffraction efficiency $T_{\lambda_i^* \lambda i}$. Detailed experimental setup information and the measured data can be found in Section S8 (Supporting Information). The SEM image reveals that the fabricated metasurface lacks the central feature (comprising 3 minor structures, as compared in Figure S7a,b, Supporting Information). To evaluate the impact of this fabrication deviation, we performed RCWA simulations on the original optimized structure (orange bars) and FDTD simulations on a modified structure without the central feature (red bars), as shown in Figure 4d. Overall, the experimental results (blue bars) show good agreement with both RCWA and FDTD simulations. We observed the reduced overall lower efficiency, ≈10% in RCWA simulations and 7% in experiments (Figure 4d). Notably, the experimental data reveal even lower diffraction efficiencies at the (−1, 1) and (1, −1) orders, a trend that is also observed in FDTD simulations and is likely caused by the missing central feature. However, analyzing the polarization states at each order (Figure S7c in Section S5, Supporting Information) confirms that the optimized
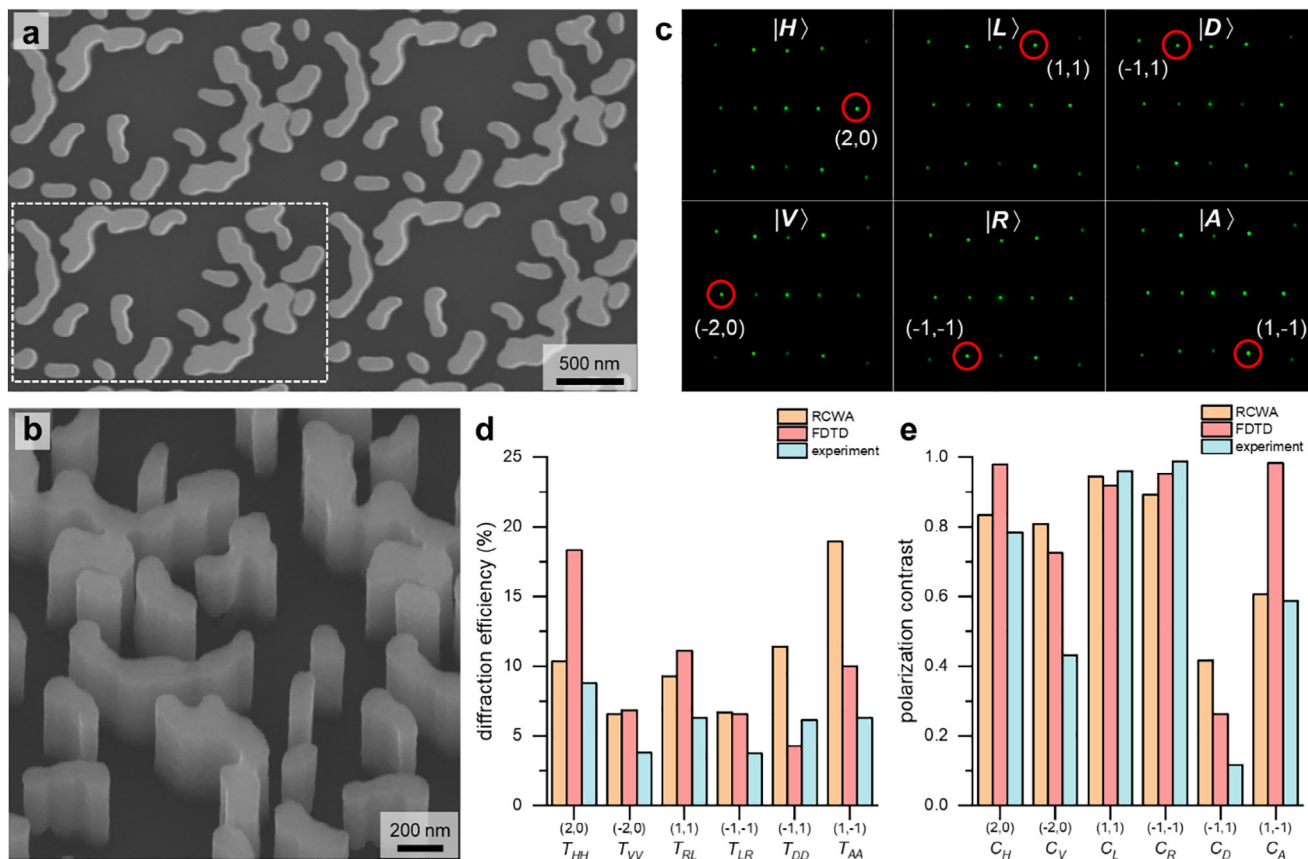
ADVANCED
SCIENCE NEWS
www.advancedsciencenews.com

ADVANCED
OPTICAL
MATERIALS
www.advopticalmat.de

Figure 4. Experimental results and analysis of the freeform metasurface for hybrid polarizations. a) SEM image of the freeform metasurface sample with the dashed line displaying one unit cell. b) Side view of the fabricated sample. c) Diffraction patterns correspond to different incident polarizations after passing through the sample, with red circles denoting the diffraction orders linked to each polarization. d) Comparison of measured (blue bar) and simulated (orange bar for RCWA simulation and red bar for FDTD simulation) diffraction efficiency. e) Comparison of measured (blue bar) and simulated (orange bar for RCWA simulation and red bar for FDTD simulation) polarization contrast. RCWA assessed the performance of the original, optimized structure, while FDTD accounted for fabrication feasibility and structure loss in the layout after the fabrication process.

polarizations still achieve higher efficiencies than non-optimized ones.

We attribute the reduced overall lower efficiency to two closely related factors. First, crosstalk is intrinsic to multi-polarization operation. Because the six diffraction channels are only partially coherent, energy inevitably leaks from the target order into neighboring ones.[23] For example, under $|H\rangle$ illumination, the (2, 0) order is the intended output, yet measurable power still appears at other orders (Figure 4c). This illustrates a fundamental functionality-versus-efficiency compromise. When we simplify the design to two channels (Section S9, Supporting Information), the diffraction efficiency rises markedly to ≈80% in simulations and 31% in experiments, confirming that fewer channels mitigate crosstalk. Second, the computational models themselves introduce approximations. In our RCWA calculations, we employed a moderate number of Fourier harmonics, while the FDTD simulations relied on a mesh of limited resolution (see Section S10, Supporting Information for details). These choices keep the runtime tractable but inevitably reduce numerical accuracy, resulting in a slight underestimation of the efficiency.

We also evaluated the polarization contrast $C_{\lambda i}$ for each diffraction order, defining it as

$$C_{\lambda i} = \left(T_{\lambda_i^* \lambda i} - T_{\lambda_{\perp i}^*, \lambda \perp i} \right) / \left(T_{\lambda_i^* \lambda i} + T_{\lambda_{\perp i}^*, \lambda \perp i} \right) \quad (4)$$

where $\lambda_{\perp i}$ denotes the orthogonal polarization state to the desired incident polarization state. A comparison of simulated and experimental results shows that the polarization contrast reaches up to 94.37% numerically at the (1, 1) order and 98.68% experimentally at the (-1, -1) order, as shown in Figure 4e. Overall, the experimental results stay in good agreement with both RCWA and FDTD simulations. A lower-than-average polarization contrast is observed at the (-1, 1) order in both the RCWA simulations of the optimized structure (orange bar) and the FDTD simulations after removing three minor features (red bar). The experimental data further reveal an even lower polarization contrast at the (−1, 1) order (see Section S5, Supporting Information for a detailed numerical comparison). Additionally, different modeling configurations in various simulation methods can have varying effects on the differences observed in experimental results and simulation data

**ADVANCED
SCIENCE NEWS**

www.advancedsciencenews.com

**ADVANCED
OPTICAL
MATERIALS**

www.advopticalmat.de

(see Section S10, Supporting Information for detailed simulation methods discussion).

5. Conclusion

In this study, we integrated forward design with inverse topology optimization to experimentally demonstrate a freeform metasurface suited for mixed-polarization applications. Our approach achieves the functionality of matrix Fourier optics, realized via forward, vector-Fourier-based design, thereby confirming the feasibility of freeform matrix Fourier optics and opening avenues for further research in polarization optics. We began by superposing three pre-designed metasurfaces, each targeting a different pair of orthogonal polarizations. This methodology positioned the design closer to a favorable local maximum, thereby improving the gradient-based topology optimization's ability to converge on an optimal solution that meets the complex mixed-polarization requirements. The resulting device exhibited notable diffraction efficiencies for six distinct polarizations, each directed to the corresponding diffraction order, with a polarization contrast reaching up to 98.68%.

Despite discrepancies between simulations and experiments, likely caused by fabrication inaccuracies that affect grating performance and different modeling configurations in distinct simulation methods, the freeform metasurface still demonstrates the potential for achieving matrix Fourier optics via topology optimization. This finding broadens the scope of potential optical applications. The high degree of design freedom can, however, increase the risk of the algorithm becoming trapped in local maxima due to increased structural complexity. Introducing physical constraints to simplify the optimization or refining the objective functions to emphasize specific polarization states could better align the design with performance goals. Furthermore, the current design exhibits limited tolerance to fabrication errors. Accounting for manufacturing variability during optimization could enhance robustness by mitigating sensitivity to process imperfections. To identify a more global optimum, combining topology optimization with machine learning may be beneficial, although this approach would require an extensive set of initial and optimized patterns for training.[42,43] Overall, our approach holds promise for expanding polarization optics to diverse fields, such as remote sensing, atmospheric science, medical diagnostics, material analysis, chemical detection, machine vision, and autonomous vehicle systems—areas where complexity has previously posed a challenge.

Supporting Information

Supporting Information is available from the Wiley Online Library or from the author.

Acknowledgements

Conflict of Interest

The authors declare no conflict of interest.

Author Contributions

Y.-W.H. initiated the study and contributed the required materials and analysis tools. Y.-C.W., Y.-T.L., and Y.-Q.Z. performed numerical calculation, topology optimization, and simulation. Y.-C.W., C.-Y.L., H.-T.S., and Y.-T.L. fabricated the metasurface samples. Y.-C.W. and C.-Y.L. performed the optical experiments. Y.-C.W., Y.-T.L., and Y.-W.H. analyzed the experimental data. Y.-T.L. and Y.-W.H. wrote the manuscript. All authors discussed the results and commented on the manuscript.

Data Availability Statement

The data that support the findings of this study are available from the corresponding author upon reasonable request.

Keywords

[1] J. W. Goodman, *Introduction to Fourier Optics*, Roberts & Co., Greenwood Village, CO, USA **2005**.

[2] T. W. Cronin, N. Shashar, R. L. Caldwell, J. Marshall, A. G. Cheroske, T.-H. Chiou, *Integr. Comp. Biol.* **2003**, *43*, 549.

[3] T. Heinloth, J. Uhlhorn, M. F. Wernet, *Front. Cell. Neurosci.* **2018**, *12*, 50.

[4] C. He, H. He, J. Chang, B. Chen, H. Ma, M. J. Booth, *Light Sci. Appl.* **2021**, *10*, 194.

[5] T. Robishaw, C. Heiles, *The WSPC Handbook of Astronomical Instrumentation*, World Scientific, Singapore **2021**, pp. 127–158.

[6] R. R. McLeod, K. H. Wagner, *Adv. Opt. Photonics* **2014**, *6*, 368.

[7] N. Yu, F. Aieta, P. Genevet, M. A. Kats, Z. Gaburro, F. Capasso, *Nano Lett.* **2012**, *12*, 6328.

[8] A. Arbabi, Y. Horie, M. Bagheri, A. Faraon, *Nat. Nanotechnol.* **2015**, *10*, 937.

[9] E. Arbabi, S. M. Kamali, A. Arbabi, A. Faraon, *ACS Photonics* **2018**, *5*, 3132.

[10] J. P. Balthasar Mueller, N. A. Rubin, R. C. Devlin, B. Groever, F. Capasso, *Phys. Rev. Lett.* **2017**, *118*, 113901.

[11] Y.-W. Huang, N. A. Rubin, A. Ambrosio, Z. Shi, R. C. Devlin, C.-W. Qiu, F. Capasso, *Opt. Express* **2019**, *27*, 7469.

[12] Z. Shi, N. A. Rubin, J.-S. Park, F. Capasso, *Phys. Rev. Lett.* **2022**, *129*, 167403.

[13] Y. Bao, F. Nan, J. Yan, X. Yang, C.-W. Qiu, B. Li, *Nat. Commun.* **2022**, *13*, 7550.

[14] A. Palmieri, A. H. Dorrah, J. Yang, J. Oh, P. Dainese, F. Capasso, *Opt. Express* **2024**, *32*, 8146.

[15] P. C. Wu, W.-Y. Tsai, W. T. Chen, Y.-W. Huang, T.-Y. Chen, J.-W. Chen, C. Y. Liao, C. H. Chu, G. Sun, D. P. Tsai, *Nano Lett.* **2017**, *17*, 445.

[16] Z.-L. Deng, J. Deng, X. Zhuang, S. Wang, K. Li, Y. Wang, Y. Chi, X. Ye, J. Xu, G. P. Wang, R. Zhao, X. Wang, Y. Cao, X. Cheng, G. Li, X. Li, *Nano Lett.* **2018**, *18*, 2885.

**ADVANCED
SCIENCE NEWS**

www.advancedsciencenews.com

**ADVANCED
OPTICAL
MATERIALS**

www.advopticalmat.de

[17] F. Ding, B. Chang, Q. Wei, L. Huang, X. Guan, S. I. Bozhevolnyi, *Laser Photonics Rev.* **2020**, *14*, 2000116.

[18] Q. Song, A. Baroni, R. Sawant, P. Ni, V. Brandli, S. Chenot, S. Vézian, B. Damilano, P. de Mierry, S. Khadir, P. Ferrand, P. Genevet, *Nat. Commun.* **2020**, *11*, 2651.

[19] N. A. Rubin, G. D'Aversa, P. Chevalier, Z. Shi, W. T. Chen, F. Capasso, *Science* **2019**, *365*, aax1839.

[20] N. A. Rubin, Z. Shi, F. Capasso, *Adv. Opt. Photonics* **2021**, *13*, 836.

[21] N. A. Rubin, A. Zaidi, A. H. Dorrah, Z. Shi, F. Capasso, *Sci. Adv.* **2021**, *7*, abg7488.

[22] A. Zaidi, N. A. Rubin, M. L. Meretska, L. W. Li, A. H. Dorrah, J.-S. Park, F. Capasso, *Nat. Photonics* **2024**, *18*, 704.

[23] B. Xiong, Y. Liu, Y. Xu, L. Deng, C.-W. Chen, J.-N. Wang, R. Peng, Y. Lai, Y. Liu, M. Wang, *Science* **2023**, *379*, 294.

[24] R. Zhang, Y. Guo, F. Zhang, M. Pu, Y. Fan, Q. Zhang, X. Li, M. Xu, J. Xu, X. Luo, *Laser Photonics Rev.* **2024**, *18*, 2400126.

[25] Z. Li, R. Pestourie, Z. Lin, S. G. Johnson, F. Capasso, *ACS Photonics* **2022**, *9*, 2178.

[26] W. Ma, Z. Liu, Z. A. Kudyshev, A. Boltasseva, W. Cai, Y. Liu, *Nat. Photonics* **2021**, *15*, 77.

[27] C.-H. Lin, S.-H. Huang, T.-H. Lin, P. C. Wu, *Nat. Commun.* **2023**, *14*, 6979.

[28] J. R. Ong, H. S. Chu, V. H. Chen, A. Y. Zhu, P. Genevet, *Opt. Lett.* **2017**, *42*, 2639.

[29] D. Z. Zhu, E. B. Whiting, S. D. Campbell, D. B. Burckel, D. H. Werner, *ACS Photonics* **2019**, *6*, 2741.

[30] C.-H. Lin, Y.-S. Chen, J.-T. Lin, H. C. Wu, H.-T. Kuo, C.-F. Lin, P. Chen, P. C. Wu, *Nano Lett.* **2021**, *21*, 4981.

[31] D. Sell, J. Yang, S. Doshay, R. Yang, J. A. Fan, *Nano Lett.* **2017**, *17*, 3752.

[32] Z. Shi, A. Y. Zhu, Z. Li, Y.-W. Huang, W. T. Chen, C.-W. Qiu, F. Capasso, *Sci. Adv.* **2020**, *6*, aba3367.

[33] H.-T. Su, L.-Y. Wang, C.-Y. Hsu, Y.-C. Wu, C.-Y. Lin, S.-M. Chang, Y.-W. Huang, *Nano Lett.* **2024**, *24*, 10055.

[34] T. Choi, C. Choi, J. Bang, Y. Kim, H. Son, C. Kim, J. Jang, Y. Jeong, B. Lee, *Nano Lett.* **2024**, *24*, 10980.

[35] M. Choi, J. Kim, S. Moon, K. Shin, S.-W. Nam, Y. Park, D. Kang, G. Jeon, K. Lee, D. H. Yoon, Y. Jeong, C.-K. Lee, J. Rho, *Nat. Mater.* **2025**, *24*, 535.

[36] C. M. Lalau-Keraly, S. Bhargava, O. D. Miller, E. Yablonovitch, *Opt. Express* **2013**, *21*, 21693.

[37] S. Kim, J. Kim, K. Kim, M. Jeong, J. Rho, *Nat. Commun.* **2025**, *16*, 411.

[38] J. P. Hugonin, P. Lalanne, *arXiv* **2025**, arXiv:210100901.

[39] J. Jiang, R. Lupoiu, E. W. Wang, D. Sell, J. P. Hugonin, P. Lalanne, J. A. Fan, *Opt. Express* **2020**, *28*, 13670.

[40] R. C. Devlin, M. Khorasaninejad, W. T. Chen, J. Oh, F. Capasso, *Proc. Natl. Acad. Sci. USA* **2016**, *113*, 10473.

[41] C.-Y. Lin, J.-H. Huang, H.-T. Su, S.-M. Chang, Y.-C. Wu, Y.-W. Huang, *Adv. Opt. Mater.* **2024**, *12*, 2401335.

[42] J. Jiang, D. Sell, S. Hoyer, J. Hickey, J. Yang, J. A. Fan, *ACS Nano* **2019**, *13*, 8872.

[43] J. Jiang, J. A. Fan, *Nano Lett.* **2019**, *19*, 5366.